

Appendix 2: Supplementary Figures

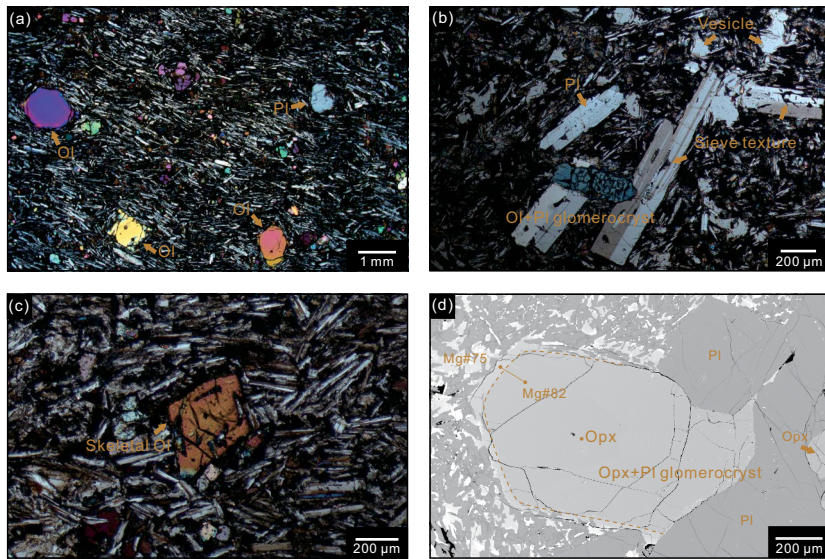


FIGURE S1. Petrographic photos of TD basalts. **(a)** Cross-polarized light (XPL) image showing plagioclase and olivine macrocrysts in a fine-grained groundmass. **(b)** XPL image showing a glomerocryst containing tabular plagioclases and embedded euhedral olivine. Plagioclase cores display sieve texture. **(c)** XPL image showing a skeletal olivine microlite in a fine-grained groundmass. **(d)** Backscattered electron (BSE) image displaying a cm-sized glomerocryst including tabular plagioclases and euhedral orthopyroxenes. Orthopyroxenes are normally zoned. Orthopyroxene cores are in contact with plagioclases in the glomerocrysts but are isolated by orthopyroxene rims from the groundmass. Abbreviations: Ol = Olivine, Pl = Plagioclase, Opx = Orthopyroxene.

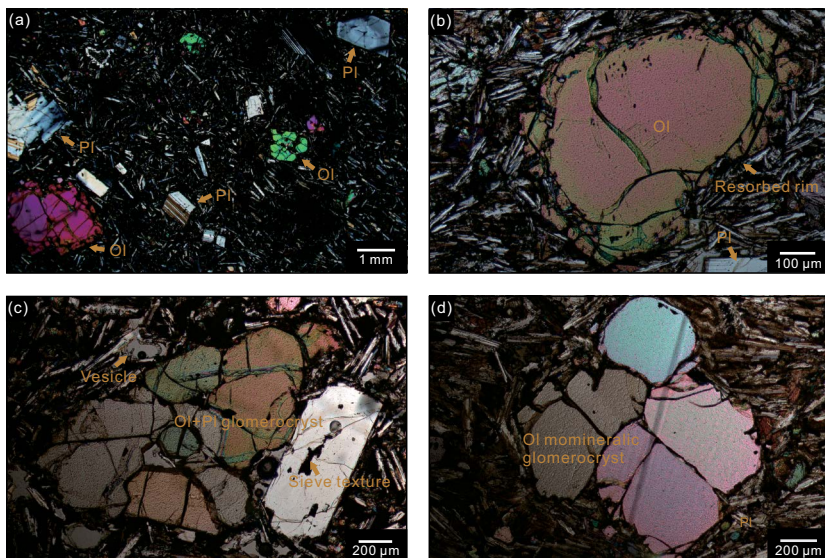


FIGURE S2. Petrographic photos of BS basalts. **(a)** XPL image illustrating plagioclases and olivine macrocrysts in a fine-grained groundmass. **(b)** XPL image showing the resorbed/embayed rims of the olivine macrocryst. **(c)** XPL image showing a glomerocryst containing subhedral olivines and tabular plagioclase. **(d)** XPL image exhibiting a glomerocryst consisting of olivines. Abbreviations are as in Fig. S1.

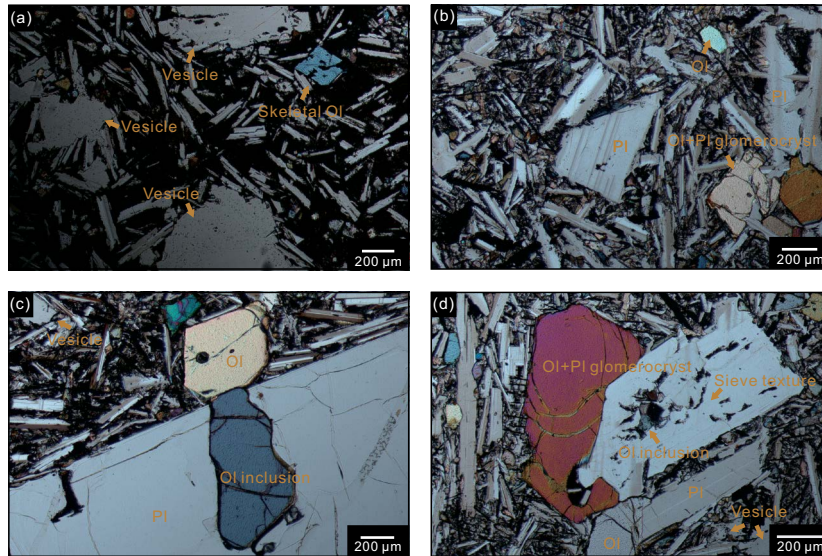


FIGURE S3. Petrographic photos of LFZ basalts. (a) XPL image illustrating nearly aphyric basalts including abundant vesicles. Skeletal olivine microlites are also found in these vesicle-rich basalts. (b) XPL image showing high crystallinity basalts containing plagioclase macrocrysts and polymineralic glomerocrysts composed of olivines and plagioclases. The plagioclases usually form the framework of the glomerocrysts, and euhedral to subhedral olivines occur within the framework as interstitial phases. (c) XPL image showing a cm-sized plagioclase macrocryst containing an olivine inclusion. (d) XPL image illustrating a glomerocryst composed of tabular plagioclase and subhedral olivine set in a coarse-grained groundmass. Plagioclase and olivine in glomerocrysts display similar sizes and the plagioclase cores display sieve texture. Abbreviations are as in Fig. S1.

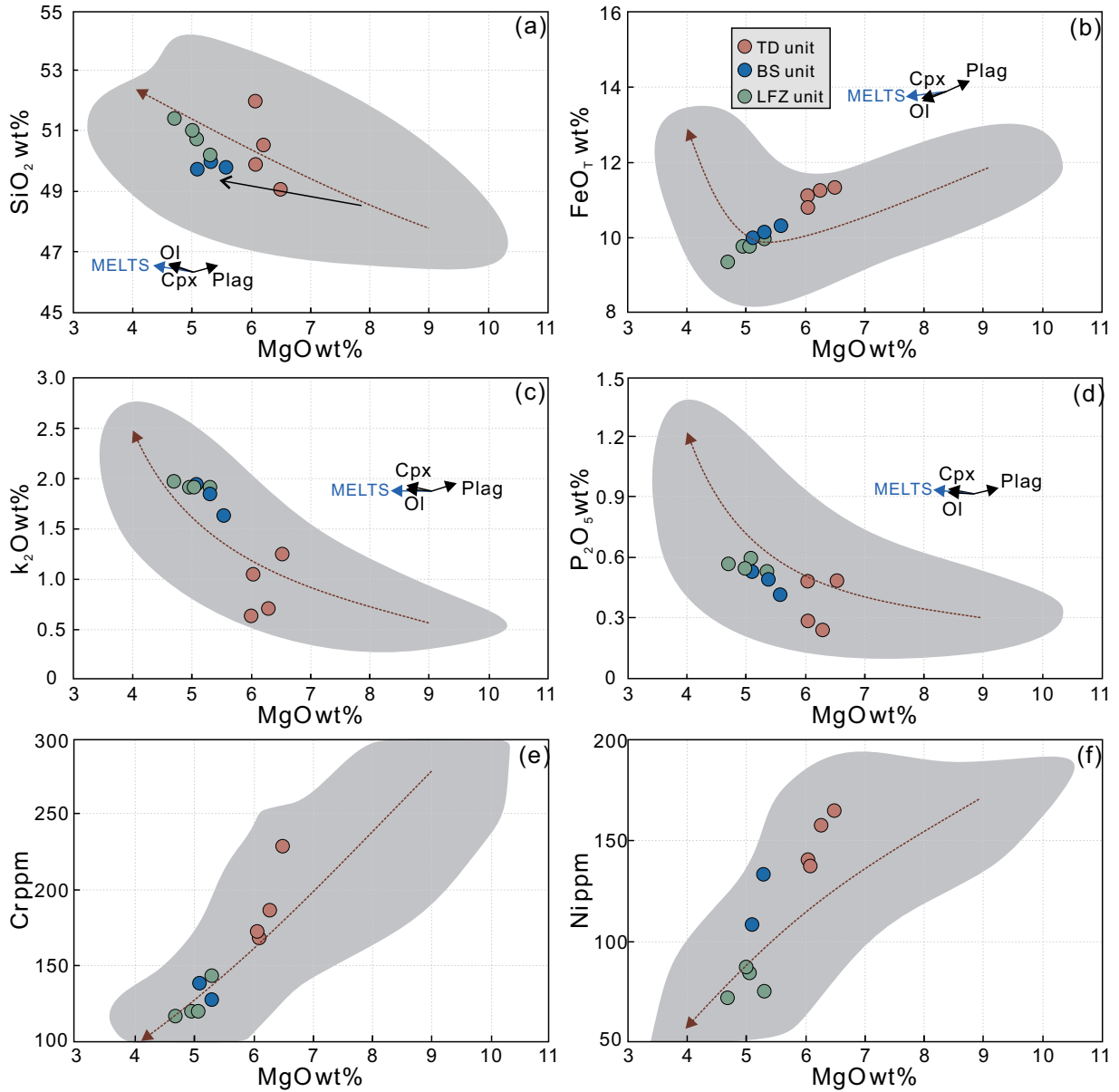


FIGURE S4. Variation diagrams of major elements (in wt%) and trace elements (in ppm) plotted against MgO contents (in wt%) for the TD, BS, and LFZ bulk-rock compositions. Black arrows indicate expected variation trends for liquid differentiation by fractionating 10% of different major phases observed in our samples. The colored arrows and shaded areas are the same as in Fig. 5.

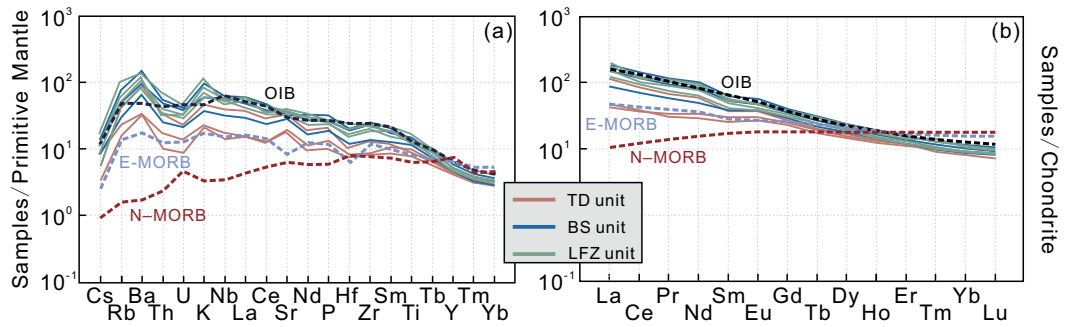


FIGURE S5. Primitive mantle normalized trace elements patterns (a) and chondrite normalized REE patterns (b) for the TD, BS, and LFZ units. The trace element data of N-type MORB are from Saunders and Tarney (1984) and Sun (1980), and the REE data are from Sun and McDonough (1989). The data for E-type MORB are from Klein (2003). The data for OIB and primitive mantle and C1 chondrite normalizing values are from Sun and McDonough (1989).

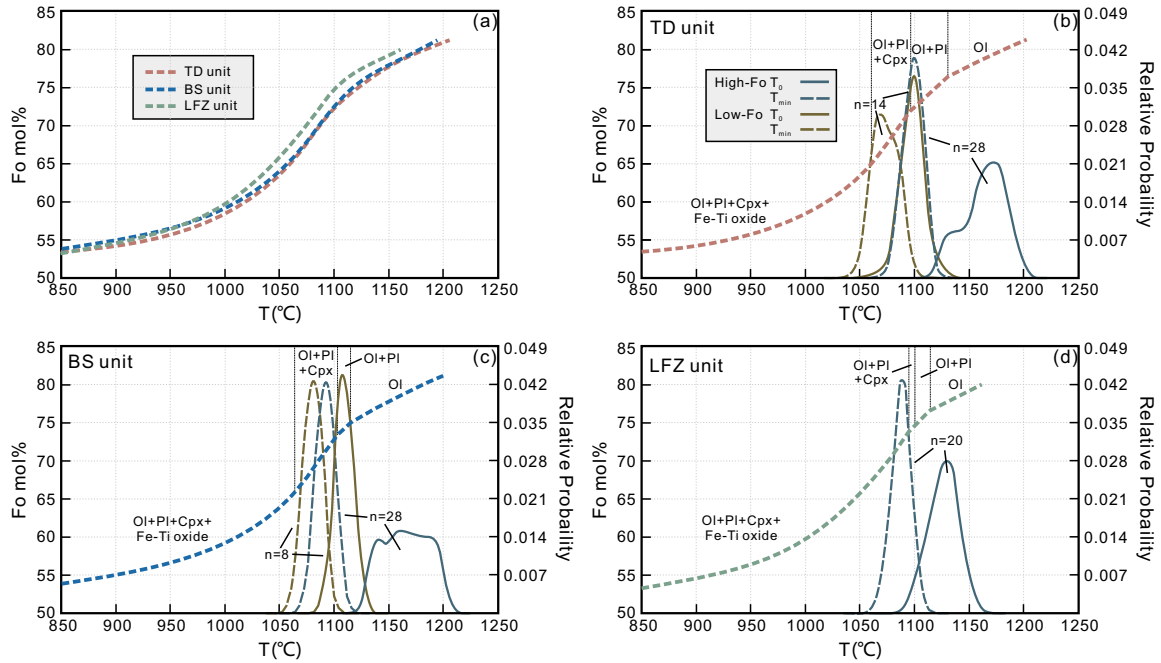


FIGURE S6. Melt evolutionary paths of olivine equilibrium composition over the temperature range 1250–850 °C for the TD, BS, and LFZ units modelled using rhyolite-MELTS. All models were conducted under 1 kbar and NNO-1 buffer. The colored lines in (b, c, d) represent the T_0 and T_{min} based on the Kernel density estimate with bandwidth 7. The results show that high-Fo populations from the TD and BS units record a large range of T_0 , varying from 1128 to 1193 °C and 1139 to 1197 °C, respectively. T_{min} from the high-Fo populations (peak at 1100 °C of the TD unit and 1094 °C of the BS unit) is similar to or slightly lower than T_0 of the low-Fo populations (peak at 1083 °C for the TD unit and 1084 °C for the BS unit) at the same unit. T_0 and T_{min} from the high-Fo population of the LFZ unit display a significant peak at 1130 °C and 1189 °C, respectively.

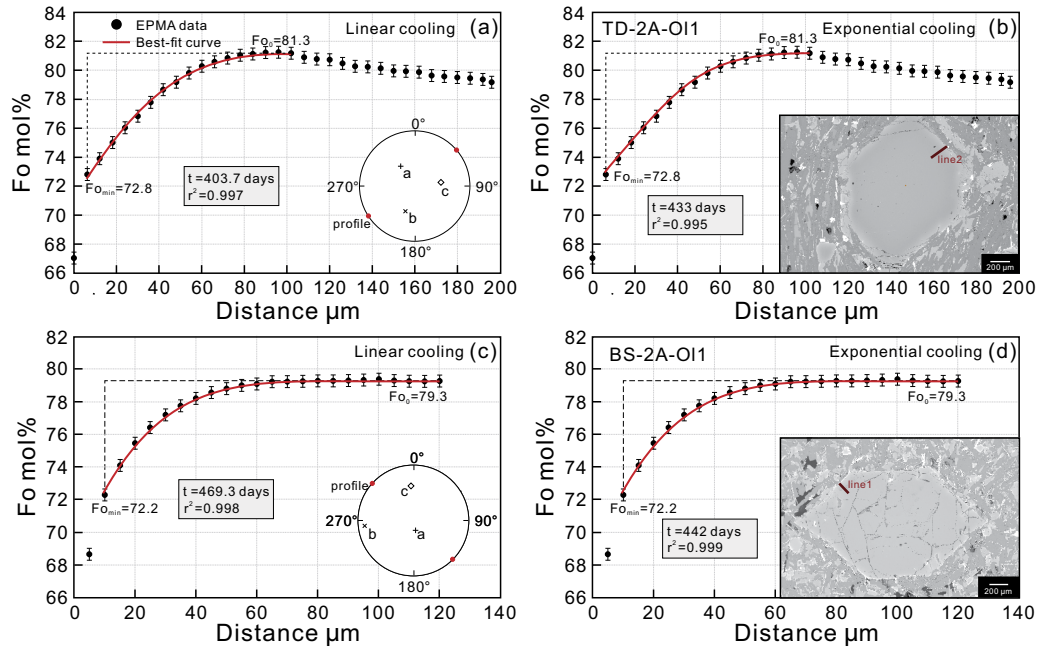


FIGURE S7. Representative BSE images, compositional profiles, and the model best-fit curves of high- Fo populations from the TD and BS units based on the linear cooling (a and c) and exponential cooling (b and d) models. BSE images and stereographic plots illustrate the location of the analytical traverses and orientation of the crystallographic axes. Red lines show best-fit curves from the dynamic diffusion model. Black dash lines indicate the assumed initial conditions. The analytical error of EPMA data is 2σ (± 0.34 mol %) in Fo contents. The results suggest that both cooling models generate well-fitting and comparable timescale results.

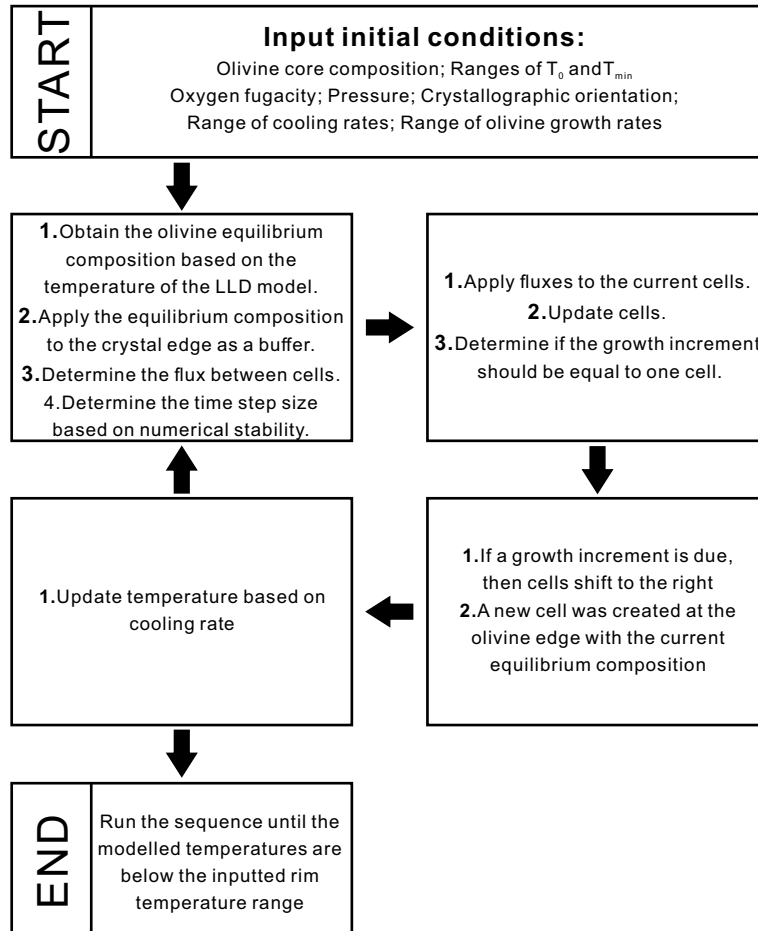


FIGURE S8. Schematic diagram showing the workflow of the dynamic diffusion model (modified from Couperthwaite et al. 2021 and Bell et al. 2023).

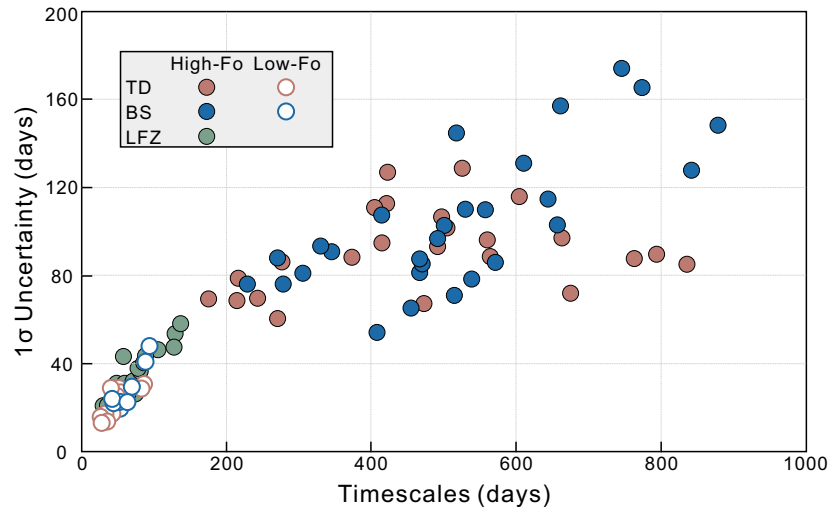


FIGURE S9. A binary graph showing the obtained timescales and their 1σ uncertainty. The variables that control the diffusivity related uncertainties include the temperature (± 20 °C), oxygen fugacity (± 0.5 log units), and olivine composition (± 1.7 mol % on Fo). The modelled results indicate that uncertainties gradually amplify with increased diffusion timescales.

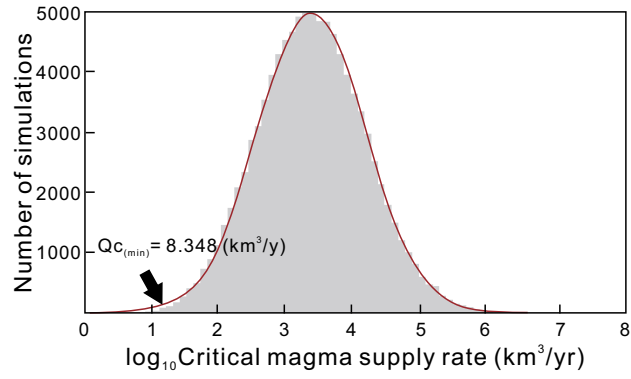


FIGURE S10. The expected range of critical magma supply rates via Monte Carlo simulations. The minimum magma supply rate (Q_c) is $8.3 \text{ km}^3/\text{yr}$.